

Cryo-EM structure of an activated GPCR-G protein complex in lipid nanodiscs

Gerhard Wagner (✉ gerhard_wagner@hms.harvard.edu)

Harvard University <https://orcid.org/0000-0002-2063-4401>

Meng Zhang

Harvard University <https://orcid.org/0000-0003-4497-3253>

Miao Gui

Harvard Medical School <https://orcid.org/0000-0001-9113-8029>

Zi-Fu Wang

Harvard University

Christoph Gorgulla

Harvard University

James Yu

Harvard University

Zhen-Yu Sun

Harvard Medical School

Christoph Klenk

University of Zurich <https://orcid.org/0000-0001-5199-7144>

Lisa Merklinger

University of Zurich

Lena Morstein

University of Zurich

Franz Hagn

Technical University Munich

Andreas Plückthun

University of Zurich <https://orcid.org/0000-0003-4191-5306>

Alan Brown

Harvard Medical School <https://orcid.org/0000-0002-0021-0476>

Mahmoud Nasr

Harvard Medical School

Hao Wu

Harvard Medical School

Keywords: Cryo-EM, structure, activated, GPCR-G, protein complex, lipid, nanodiscs

Posted Date: September 2nd, 2020

DOI: <https://doi.org/10.21203/rs.3.rs-57572/v1>

License:  This work is licensed under a Creative Commons Attribution 4.0 International License.

[Read Full License](#)

Version of Record: A version of this preprint was published at Nature Structural & Molecular Biology on February 25th, 2021. See the published version at <https://doi.org/10.1038/s41594-020-00554-6>.

Abstract

G protein coupled receptors (GPCRs) are the largest superfamily of transmembrane proteins and the targets of over 30% of currently marketed pharmaceuticals. Although several structures have been solved for GPCR-G protein complexes, structural studies of the complex in a physiological lipid membrane environment are lacking. Here, we report cryo-EM structures of lipid bilayer-bound complexes of neurotensin, neurotensin receptor 1, and $G_{\alpha_1}\beta_1\gamma_1$ protein in two conformational states, resolved to 4.1 and 4.2 Å resolution. The structures were determined in lipid bilayer without any stabilizing antibodies/nanobodies, and thus provide a native-like platform for understanding the structural basis of GPCR-G protein complex formation. Our structures reveal an extended network of protein-protein interactions at the GPCR-G protein interface compared to in detergent micelles, defining roles for the lipid membrane in modulating the structure and dynamics of complex formation, and providing a molecular explanation for the stronger interaction between GPCR and G protein in lipid bilayers. We propose a detailed allosteric mechanism for GDP release, providing new insights into the activation of G proteins for downstream signaling.

Introduction

G protein coupled receptors (GPCRs) sense extracellular stimuli including odorants, hormones, neurotransmitters, and photons^{1,2}. A stimulus leads to a shift in the conformational equilibrium of the GPCR towards a state which favors binding of the intracellular signal transducer, GDP-bound heterotrimeric G $\alpha\beta\gamma$ protein³. Binding causes perturbation of the GDP binding pocket, leading to replacement of GDP by GTP and the dissociation of the G α and G $\beta\gamma$ subunits from each other and the GPCR⁴. The released G α and G $\beta\gamma$ subunits remain anchored to the membrane through lipid modifications but diffuse and interact with downstream effectors to stimulate signaling cascades³.

Recent advances in X-ray crystallography and cryo-EM have allowed the determination of several GPCR-G protein complex structures to near-atomic resolution^{5,6,15-18,7-14}. However, due to difficulties in preparing stable GPCR-G protein complexes in detergent micelles, a range of stabilization techniques had to be employed for most of the structures reported so far, including binding to antibodies or nanobodies, dominant-negative G α (DN $G\alpha$) subunits, or mini-G proteins that lack the α -helical domain (AHD) of G α . Furthermore, the majority of previous structural studies reconstituted GPCR-G protein complexes in detergent micelles, with the only exception being a recently published structure of D2 dopamine receptor in complex with a dominant negative G β_1 and a stabilizing antibody scFv16 in lipid nanodiscs¹⁹. The detergent structures fail to replicate the properties of the native lipid bilayer environment of GPCRs, including membrane thickness, lateral pressure, and curvature²⁰. It has been reported that various GPCRs exhibit higher stability and better functionality when incorporated into lipid bilayers as compared to detergent micelles^{21,22}. Additionally, negatively charged lipids have been found to allosterically modulate GPCR activation and its selective interaction with G proteins²³⁻²⁵. Therefore, structural and dynamical

information for the GPCR–G protein interaction in a lipid bilayer environment is necessary to understand the GPCR signal transduction mechanism.

To investigate the interaction between GPCR and G proteins in lipid bilayers, we used the neurotensin receptor 1 (NTR1)-G_i interaction as a model system. NTR1 is a class A GPCR that responds to neurotensin (NT), a 13-residue peptide implicated in the pathogenesis of schizophrenia, antinociception, hypothermia, Parkinson's disease and tumor growth^{1,26}. To reconstitute and determine the structure of the NT₈₋₁₃-NTR1-Ga_{i1}b₁g₁ complex in a lipid bilayer environment we used circularized nanodiscs (cNDs) prepared with covalently circularized membrane scaffold proteins²⁷, which also allowed structure determination in the absence of external stabilizing factors. While structures of the GDP-bound G protein heterotrimer²⁸ and most GPCR-G protein complexes were so far only available in detergent micelles, such as the recent cryo-EM structure of the NTR1-Ga_{i1}b₁g₂ complex stabilized by scFv16 and in complex with a pseudopeptide analog of NT⁸, the data shown here provide insights into the mechanism by which a G protein is activated by the interaction with GPCR in a lipid bilayer.

Results

Lipid bilayers enhance the efficiency of NT-NTR1-Ga_{i1}b₁g₁ complex formation

To enable efficient expression of NTR1 for purification and structural studies, we took advantage of the TM86V-L167R DIC3B construct²⁹. Compared to the inactive TM86V construct, TM86V-L167R contains a back mutation of L167R which restores the functionality of NTR1 (ref. ³¹). The TM86V-L167R DIC3B²⁹ exhibits similar downstream signaling functionality to wild-type NTR1 as measured by the production of inositol-1-phosphate (IP1), the final metabolite of the inositol phosphate cascade, with a EC₅₀ of 2.7 nM for wild-type NTR1 and 0.22 nM for TM86V-L167R DIC3B (Extended Data Fig. 1a, left). The single mutation of R167^{3.50}L (superscripts denote Ballesteros–Weinstein numbering³⁰) in the TM86V construct completely quenched IP1 production (Extended Data Fig. 1a, right). As we discuss later, R167^{3.50} directly interacts with G_i in the complex structures determined in this study, explaining partially the critical impact of this residue in the signaling process.

NTR1 was affinity purified using immobilized NT₈₋₁₃, which ensured selection of properly folded NTR1 only. The purified NT-NTR1 complex was then incorporated into 9-nm diameter covalently circularized nanodiscs (cNDs), containing a mixture of zwitterionic lipid POPC and negatively charged lipid POPG, and belted by circularized membrane scaffold protein cNW9 (ref.²⁷) (Fig. 1a and Extended Data Fig. 1). Heat-treating the purified nanodiscs at 42 °C for 24 hours improved sample homogeneity (Extended Data Fig. 1c). Circular dichroism measurements showed increased thermostability of NTR1 in cNDs as compared to in detergent micelles, with a transition temperature about 18 °C higher (Fig. 1b and Extended Data Fig. 2a, b), implying different dynamic properties in lipid bilayer relative to in detergents. The sample

was stable at 45 °C for at least 15 days, showing well dispersed and reproducible peaks on two-dimensional nuclear magnetic resonance (2D NMR) spectra (Extended Data Fig. 3a). These observations agree with studies showing that GPCRs are more stable in membrane environments³¹. When Ga_{i1}b₁g₁ was incorporated into cNDs using the same method, its thermostability also improved relative to in detergent micelles (Extended Data Fig. 2d-f).

To reconstitute the signaling complex, we incubated NT-NTR1-cND with wild-type heterotrimeric human Ga_{i1}b₁g₁, which is myristoylated on Ga_{i1} and prenylated on Gg₁ (Extended Data Fig. 1d). The NT-NTR1-Ga_{i1}b₁g₁ complex in cNDs exhibits high thermostability (Fig. 1b and Extended Data Fig. 2c), and the binding affinity of NTR1 to Ga_{i1}b₁g₁ is higher in cNDs than in detergent micelles (K_D of 76 nM compared to 1.4 mM) (Fig. 1c), reflecting the essential role the membrane plays in efficient GPCR-G protein complex formation. Further binding kinetic measurements revealed two binding modes in cNDs with K_D of 5.8 nM and 38 nM, respectively (Fig. 1d and Extended Data Fig. 4a, b). The complex in cND is capable of GDP/GTP exchange, as shown by a much higher dissociation rate upon addition of GTPγS (Extended Data Fig. 4c). However, for the following structural studies, we used apyrase to hydrolyze free GDP, which stabilizes the NT-NTR1-Ga_{i1}b₁g₁ complex.

Cryo-EM structure of the NT-NTR1-Ga_{i1}b₁g₁ complex in cNDs

The higher affinity and improved thermostability of the NT-NTR1-Ga_{i1}b₁g₁ complex in lipid bilayers relative to in detergent micelles allowed us to collect cryo-EM data (Fig. 2, Extended Data Fig. 5) for the complexes without the need for further stabilization by antibodies/nanobodies or engineered G proteins. Two-dimensional class averages showed intact complexes within cNDs with uniform 9-nm diameters (Extended Data Fig. 5). Three-dimensional classification of these projections revealed two well-resolved classes, corresponding to “canonical” (C) and “noncanonical” (NC) states of the NT-NTR1-Ga_{i1}b₁g₁ complex, at 4.3 and 4.5 Å resolution, respectively (Extended Data Fig. 5). Two conformational states were also seen in the recent cryo-EM study of the scFv16-stabilized NTR1-Ga_{i1}b₁g₂ complex in detergent micelles⁸, but, as we describe below, these states are different from those that we observe (Fig. 2c). Additional density surrounds NTR1, corresponding to the cNW9 membrane scaffold protein and the lipid bilayer it encloses. Masking out these densities improved the resolutions of the C and NC states to 4.1 Å and 4.2 Å respectively (Extended Data Fig. 5). In these maps, the pitch of helices and many sidechains are clearly resolved (Extended Data Fig. 6), allowing us to confidently place and remodel known atomic models of NT, NTR1²⁹ and Ga_{i1}b₁g₁ (ref. ^{9,30}). The density of NT is well resolved in both conformations (Extended Data Fig. 6), and adopts similar structure and interactions to those observed in detergent micelles^{8,33}. The N-terminal helices of Gb and Gg both show weak densities, presumably due to flexibility.

Compared to most reported structures^{7-14,17,18}, the α-helical domain (AHD) of Ga_{i1} is clearly resolved in both states (Fig. 2a, Extended Data Fig. 7a, b). In the few structures that do report the position of the

AHD^{5,6,16}, the position may be affected by crystal contacts and/or the nanobodies/antibodies that were included for stabilization (Extended Data Fig. 7c-f). Our structures lack these constraints and therefore more closely reflect the native orientation and localization of the AHD in the nucleotide-free state. In comparison to the crystal structure of the GDP-bound G_i trimer²⁸, the AHD moves away from its close association with the Ras-like domain of G_α and interacts with the outer strands of the second and third β blades of G_β after GDP release (Fig. 2b, Extended Data Fig. 7a-c). As we discuss later, the large-scale movement of AHD is an important step in the GDP release pathway.

Lipid bilayer modulates GPCR-G protein interaction

The NT-NTR1-G_{α_{i1}β₁γ₁} complex shows clear interactions with the lipid bilayer in both the C and NC states (Fig. 3a, Extended data Fig. 8). Density at the beginning of the αN-helix of G_α is observed protruding into the lipid bilayer, which corresponds to the myristoylation site of the G_α (Fig. 3b, top panel). Similar density at the C-terminus of G_γ corresponds to the prenylation site (Fig. 3b, top panel). These lipid moieties anchor the G protein to the membrane. Lipid density is also observed above the positively charged αN-helix of G_α (Fig. 3b, bottom panel). The sidechains of arginine and lysine residues within this helix are oriented towards the membrane and likely form electrostatic interactions with the negatively charged lipid POPG (Fig. 3b, bottom panel). This observation agrees with the finding that negatively charged lipids strengthen the interaction between NTR1 and G protein²⁵. In comparison with other structures of class A GPCR-G_i complexes, the αN-helices of C and NC states solved here are located close to the membrane, while they bend away in structures determined in detergent micelles (Fig. 3c). The observed hydrophobic and electrostatic interactions ensure close proximity of G_i to NTR1, and thus enhance G_i binding to NTR1, particularly between the αN-β1 hinge of G_i and ICL2 of NTR1 as described below (Fig. 4a).

As expected, the majority of NTR1 is buried inside the lipid bilayer, including TM1-4 and TM7, the N-terminal half of TM5, and the C-terminal half of TM6. ICL2 and H8 are partially buried at the membrane surface (Extended Data Fig. 8c). To reveal the effects of the lipid bilayer on the GPCR, we compared our structures with the crystal structure of NTR1 (X-rNTR1)³³ and the cryo-EM structure of NTR1 in the canonical state (C-hNTR1)⁸ (representing structures of agonist-bound NTR1 in detergent in the absence and presence of G_i, respectively). In lipid bilayers, the core of NTR1 is more compact due to an inward movement of the middle of TM6 (Fig. 3d, Extended Data Fig. 9a), whereas X-rNTR1 and C-hNTR1 superpose well with each other (Extended Data Fig. 9b). Compression of TM6 is likely due to lateral pressure from the lipid bilayer. Relative to the detergent structures, ICL2 and the cytoplasmic side of TM7 and H8 show an upward movement, indicative of membrane association (Fig. 3d, Extended Data Fig. 9a). Overall, the increased compaction and better membrane association of NTR1 agrees with the improved thermostability observed in lipid bilayers (Fig. 1b, Extended Data Fig. 2c).

Upon insertion of the α5 helix of G_α into the core of NTR1, the cytoplasmic side of TM5, TM6 and ICL3 move outward to accommodate the α5 helix (Fig. 3d). Structural and dynamical changes are also

observed in 2D NMR experiments on $^1\text{H}^{15}\text{N}$ -NTR1 upon binding to G_i in cNDs (Extended Data Fig. 3c). In the presence of the lipid bilayer, this movement appears to be more restricted than the large outward movement observed in detergent, potentially due to the lateral pressure from the lipid bilayer (Fig. 3e). The reduced movement of TM5 and TM6 relative to C-hNTR1 maintains closer contacts with the $\alpha 5$ helix (Fig. 3e). Comparison of TM6 positions among class A GPCR- G_i complexes reveals that TM6 in the C-state NTR1 exhibits closest proximity to the $\alpha 5$ helix, resulting in more potential interactions (Fig. 3f and Extended Data Fig. 9c). Taken together, these observations suggest that the lipid bilayer constrains the conformation of NTR1 to enhance its interaction with G_i , agreeing with our observation of higher binding affinity in lipid bilayer (Fig. 1c).

The NTR1- $G_{\alpha_1}\beta_1\gamma_1$ interface

The C and NC states are related by a 50° rotation of G_i relative to NTR1 (Fig. 4a). This change in orientation results in different interactions between the αN helix and ICL2. In the C state, a potential salt bridge is observed between E28 and R185^{4.41}, as well as several potential hydrogen bonds between E28 and S182^{4.38}, R32 and T179^{34.55}, and A31 and K178^{34.54} (Fig. 4a). In contrast, only one hydrogen bond (between R32 and T178^{34.55}) is observed in C-hNTR1 in detergent micelles⁸. These additional contacts with ICL2 in the presence of the lipid bilayer likely result from the closer proximity of the αN helix to the membrane and NTR1 (Fig. 3c). Many of these interactions are absent in the NC state, where we observe only one potential salt bridge between E28 and K176^{34.52}. Fewer contacts in the NC state suggest that it could be a less stable intermediate state before the C-state complex.

The orientation of the $\alpha 5$ helix relative to NTR1 is also different between the two states, although the depth of insertion is the same (Fig. 4b). In the C state, several potential hydrogen bonds are observed, including C351 with E166^{3.49}, C351 with R167^{3.50}, and N347 with A170^{3.53} (Fig. 4b). The interaction between N347 and A170^{3.53} is also observed in C-hNTR1⁸. E166^{3.49} and R167^{3.50} belong to the highly conserved D/ERY motif. R167^{3.50} is found to be essential for downstream signaling (Extended Data Fig. 1a) and has been reported to be critical for GDP/GTP exchange through mutagenesis studies²⁹. Examination of a range of class A GPCR- G_i structures shows that it is common for $\alpha 5$ insertion to stop at R^{3.50} (Extended Data Fig. 10d). Thus, R^{3.50} might serve as both an interaction hot-spot and an “access gate” that decides the depth of $\alpha 5$ insertion. The NC state displays fewer interactions with only one possible hydrogen bond between C351 and R167^{3.50} (Fig. 4b).

Rotation of G_i also results in the $\beta 6\alpha 4$ loop moving closer to ICL3 in the C state than in either the NC state (Fig. 4c) or detergent structures (Extended Data Fig. 10b). Although the map quality of ICL3 prevents a detailed analysis, molecular dynamics simulations show potential salt bridges and hydrogen bonds forming between ICL3 and $\beta 6\alpha 4$ loop in the C state (Extended Data Fig. 11). Similar interactions between

ICL3 and the b6a4 loop have been observed in the structure of the adenosine A1 receptor (A₁R)-Ga_{i2}b₁g₂ complex¹².

An insertion-rotation model for G_i activation

Comparison of our two conformational states with one another and with previous structures allows us to propose a mechanism of G-protein activation in a lipid environment. The presence of more GPCR-G_i contacts in the C state than the NC state, suggests that the NC state might be an intermediate, lower-affinity state. This implies that in addition to the close proximity between GPCR and G_i regulated by lipid bilayer, a certain orientation of G_i relative to GPCR is also required to enable efficient complex formation. This is consistent with our kinetics experiments which showed both high (5.8 nM) and lower affinity (38 nM) binding modes (Fig. 1d and Extended Data Fig. 4). A sequential model was also proposed to link the states observed with scFv16-stabilized hNTR1-G_i in detergent micelles⁸. Following this hypothesis, it appears that the interaction between NTR1 and G_i goes through an insertion-rotation mechanism (Fig. 4i). NTR1 and G_i first laterally diffuse in membrane until they meet. The cavity in NTR1 allows insertion of the a5 helix into the open core of NTR1. Subsequently, G_i rotates around a5 by approximately 50°, which maximizes protein-protein interactions (Fig. 4, Extended Data Fig. 10). The rotation stops when the b6a4 loop collides with ICL3, the aN-b1 hinge is caught by ICL2, and the a5 helix forms most contacts with the core of NTR1. As the a5 helix in the NT-NTR1-Ga_{i1}b₁g₁ C state exhibits one of the far-most rotated positions among class A GPCR-G_i complexes (Extended Data Fig. 10d), the NT-NTR1-Ga_{i1}b₁g₁ C state likely represents the final state enabling GDP dissociation (Fig. 4i).

Multiple NTR1-G_i interactions stimulate the dissociation of GDP

Based on comparison of our structures with the structure of GDP-Gi²⁸, we propose a multipartite mechanism for receptor-catalyzed nucleotide exchange that is supported by prior functional studies (Fig. 5). In the unbound G-protein, the nucleotide is buried between the ras-homology domain (RHD) and the AHD of Ga. It has been suggested that when G protein encounters the receptor, a5 helix is straightened and forms early interactions with the GPCR, which initiates the GDP release process³⁴. The AHD dissociates from the RHD, and, as we show here, interacts with the outermost strands of Gb (Extended Data Fig. 7a, b). Previous computational simulations have shown that separation of the AHD is necessary (presumably to create an exit pathway for GDP) but not sufficient for rapid nucleotide release^{35,36}. Here we observe that multiple allosteric pathways converge on structural rearrangement of the GDP binding site, and it is the combination of these pathways that are responsible for GDP dissociation.

In the first pathway, insertion and rotation of the a5 helix into the core of NTR1 by two helical turns compared to the GDP-G_i structure²⁸ displaces the a5b6 loop, which is responsible for binding the guanine

ring of GDP in the nucleotide-bound state (Fig. 4e). This is consistent with structural studies showing that the a5b6 loop perturbation induced by the rotational translation of a5 helix is essential for GDP dissociation^{5,6,16–18,32,37,38,7–14}. As a result of this perturbation, A326 in the highly conserved TCAT motif moves away from its position in the GDP-G_i structure resulting in loss of contact with GDP. This agrees with a previous mutagenesis study showing that A326 is essential for GDP binding³⁹. The conformation of the a5b6 loop is different from that in the detergent structure, potentially as a result of the different angles with which the a5 helix inserts into NTR1 (Extended Data Fig. 10c, d). This agrees with computational simulations in which the tilt angle of the a5 helix was found to directly correlate with the conformation of the a5b6 loop³⁶. The new conformation of the a5b6 loop, and therefore the dynamics of GDP loss, may be affected by the neighboring interaction between ICL3 and the b6a4 loop (Fig. 4c, e, Extended data Fig. 11).

In the second pathway, displacement of AHD causes movement of the a1 helix to which it is tethered (Fig. 4f, g). This lateral movement causes residues within a1, including S47, to dissociate from the phosphate group of GDP (Fig. 4f, g). The S47N mutation is dominant negative¹⁸, suggesting that this movement is a key step towards GDP release. Furthermore, previous mutagenesis⁴⁰, hydrogen-deuterium exchange mass spectrometry (HDX)³⁷ and computational⁴¹ studies have all suggested that perturbations in a1 play important roles in accelerating GDP dissociation.

In the third pathway, the interaction between ICL2 of NTR1 and the aN-b1 hinge propagates through the b1 strand and perturbs the GDP phosphate-binding P-loop (a1b1 loop) (Fig. 4d). P-loop perturbation by the aNb1-ICL2 interaction is also supported by previous structural^{6,10,11} and HDX³⁷ studies. This perturbation results in a displacement of the P-loop, breaking the interaction between the mainchain of residue A41 and the b-phosphate of GDP (Fig. 4d). To accommodate the displaced P loop, the sidechain of E245 on a2 has rotated by 95° (Fig. 4h). This implies a coupling of P-loop disorder with E245 rotation in the GDP dissociation process, and conversely a role for E245 in maintaining a stable GDP-bound G protein conformation, which coincides with the E245A mutant having a dominant negative effect^{12,39}. This rotation is not observed in the detergent-embedded NTR1-G_i structure, as the P loop adopts a conformation more similar to the one observed in the GDP-G_i structure²⁸ (Fig. 4h).

Together, this multi-point coordination mechanism leads to dissociation of GDP from G_i and the creation of a free nucleotide binding pocket for GTP association (Fig. 5).

Discussion

Understanding the structural basis for the interaction between GPCRs and G proteins under physiological conditions has been challenging due to the poor stability of the complexes in detergent micelles. Most of the published structures required antibodies/nanobodies and/or engineered G proteins for additional

stability, which rendered the complexes incapable of GDP/GTP exchange. Using our recently developed covalently circularized nanodiscs²⁷, we have determined two structures, representing different conformational states, of the NT-NTR1-G $\alpha_{i1}\beta_1\gamma_1$ complex in a lipid bilayer without the need for external stabilization. These structures show that the sideways movement of TM6, which is considered a signature of active receptors in detergents, is restricted by the membrane, highlighting the importance of the membrane in modulating the dynamics of GPCR-G protein interactions and the affinity between NTR1 with G $_i$. Our structures also allowed us to unravel the interconnected roles of membrane-protein interaction, G-protein activation, and GDP dissociation. The proposed multipartite allosteric mechanism of GDP release reveals a competition between GDP and NTR1 for binding G $_i$, which explains why the NTR1-G $_i$ complex is stabilized by removal of GDP using apyrase. This observation agrees with a previous NMR study showing that the interaction between NTR1 and G α is strongest when G α is nucleotide free⁴². Our study therefore provides new insights into the signal transduction process triggered by GPCR-G protein complex formation and will serve as a model for future studies of GPCR signaling in lipid bilayers.

References

1. Griebel, G. & Holsboer, F. Neuropeptide receptor ligands as drugs for psychiatric diseases: The end of the beginning? *Nature Reviews Drug Discovery* **11**, 462–478 (2012).
2. Shimada, I., Ueda, T., Kofuku, Y., Eddy, M. T. & Wüthrich, K. GPCR drug discovery: Integrating solution NMR data with crystal and cryo-EM structures. *Nature Reviews Drug Discovery* **18**, 59–82 (2018).
3. Hilger, D., Masureel, M. & Kobilka, B. K. Structure and dynamics of GPCR signaling complexes. *Nat. Struct. Mol. Biol.* **25**, 4–12 (2018).
4. Du, Y. *et al.* Assembly of a GPCR-G Protein Complex. *Cell* **177**, (2019).
5. Qi, X. *et al.* Cryo-EM structure of oxysterol-bound human Smoothed coupled to a heterotrimeric G $_i$. *Nature* (2019). doi:10.1038/s41586-019-1286-0
6. Rasmussen, S. G. F. *et al.* Crystal structure of the β 2 adrenergic receptor-Gs protein complex. *Nature* **477**, 549–557 (2011).
7. García-Nafría, J., Lee, Y., Bai, X., Carpenter, B. & Tate, C. G. Cryo-EM structure of the adenosine A2A receptor coupled to an engineered heterotrimeric G protein. *Elife* **7**, (2018).
8. Kato, H. E. *et al.* Conformational transitions of a neurotensin receptor 1–G $i1$ complex. *Nature* **572**, 80–85 (2019).
9. García-Nafría, J., Nehmé, R., Edwards, P. C. & Tate, C. G. Cryo-EM structure of the serotonin 5-HT1B receptor coupled to heterotrimeric G $_o$. *Nature* **558**, 620–623 (2018).
10. Zhang, Y. *et al.* Cryo-EM structure of the activated GLP-1 receptor in complex with a G protein. *Nature* **546**, 248–253 (2017).
11. Liang, Y. L. *et al.* Phase-plate cryo-EM structure of a class B GPCR-G-protein complex. *Nature* **546**, 118–123 (2017).

12. Draper-Joyce, C. J. *et al.* Structure of the adenosine-bound human adenosine A1 receptor-Gi complex. *Nature* **558**, 559–563 (2018).
13. Koehl, A. *et al.* Structure of the μ -opioid receptor-G i protein complex. *Nature* **558**, 547–552 (2018).
14. Krishna Kumar, K. *et al.* Structure of a Signaling Cannabinoid Receptor 1-G Protein Complex. *Cell* **176**, 448-458.e12 (2019).
15. Zhao, L.-H. *et al.* Structure and dynamics of the active human parathyroid hormone receptor-1. *Science (80-.)*. **364**, 148–153 (2019).
16. Kang, Y. *et al.* Cryo-EM structure of human rhodopsin bound to an inhibitory G protein. *Nature* **558**, 553–558 (2018).
17. Liang, Y. L. *et al.* Cryo-EM structure of the active, G s -protein complexed, human CGRP receptor. *Nature* **561**, 492–497 (2018).
18. Liang, Y. L. *et al.* Phase-plate cryo-EM structure of a biased agonistbound human GLP-1 receptor-Gs complex. *Nature* **555**, 121–125 (2018).
19. Yin, J. *et al.* Structure of a D2 dopamine receptor–G-protein complex in a lipid membrane. *Nature* **2020**, (2020).
20. Lee, A. G. How lipids affect the activities of integral membrane proteins. *Biochimica et Biophysica Acta - Biomembranes* **1666**, 62–87 (2004).
21. Whorton, M. R. *et al.* Efficient coupling of transducin to monomeric rhodopsin in a phospholipid bilayer. *J. Biol. Chem.* **283**, 4387–94 (2008).
22. Kofuku, Y. *et al.* Functional dynamics of deuterated β 2-adrenergic receptor in lipid bilayers revealed by NMR spectroscopy. *Angew. Chemie - Int. Ed.* **53**, 13376–13379 (2014).
23. Strohman, M. J. *et al.* Local membrane charge regulates β 2 adrenergic receptor coupling to G i3. *Nat. Commun.* **10**, (2019).
24. Yen, H.-Y. *et al.* PtdIns(4,5)P2 stabilizes active states of GPCRs and enhances selectivity of G-protein coupling. *Nature* **559**, 423–427 (2018).
25. Inagaki, S. *et al.* Modulation of the Interaction between Neurotensin Receptor NTS1 and Gq Protein by Lipid. *J. Mol. Biol.* **417**, 95–111 (2012).
26. Kitabgi, P. Targeting neurotensin receptors with agonists and antagonists for therapeutic purposes. *Curr. Opin. Drug Discov. Devel.* **5**, 764–76 (2002).
27. Nasr, M. L. *et al.* Covalently circularized nanodiscs for studying membrane proteins and viral entry. *Nat. Methods* **14**, 49–52 (2016).
28. Wall, M. A. *et al.* The structure of the G protein heterotrimer Gi alpha 1 beta 1 gamma 2. *Cell* **83**, 1047–58 (1995).
29. Egloff, P. *et al.* Structure of signaling-competent neurotensin receptor 1 obtained by directed evolution in *Escherichia coli*. *Proc. Natl. Acad. Sci.* **111**, E655–E662 (2014).
30. Ballesteros, J. A. & Weinstein, H. Integrated methods for the construction of three-dimensional models and computational probing of structure-function relations in G protein-coupled receptors.

Methods Neurosci. **25**, 366–428 (1995).

31. Knepp, A. M., Grunbeck, A., Banerjee, S., Sakmar, T. P. & Huber, T. Direct Measurement of Thermal Stability of Expressed CCR5 and Stabilization by Small Molecule Ligands. *Biochemistry* **50**, 502–511 (2011).
32. Gao, Y. *et al.* Structures of the Rhodopsin-Transducin Complex: Insights into G-Protein Activation. *Mol. Cell* **75**, 781-790.e3 (2019).
33. Krumm, B. E., White, J. F., Shah, P. & Grisshammer, R. Structural prerequisites for G-protein activation by the neurotensin receptor. *Nat. Commun.* **6**, 7895 (2015).
34. Liu, X. *et al.* Structural Insights into the Process of GPCR-G Protein Complex Formation. *Cell* **177**, 1243-1251.e12 (2019).
35. Dror, R. O. *et al.* Structural basis for nucleotide exchange in heterotrimeric G proteins. *Science* (80-). **348**, 1361–1365 (2015).
36. Sun, X., Singh, S., Blumer, K. J. & Bowman, G. R. Simulation of spontaneous G protein activation reveals a new intermediate driving GDP unbinding. *Elife* **7**, (2018).
37. Chung, K. Y. *et al.* Conformational changes in the G protein Gs induced by the β 2 adrenergic receptor. *Nature* **477**, 611–617 (2011).
38. Erlandson, S. C., McMahon, C. & Kruse, A. C. Structural Basis for G Protein–Coupled Receptor Signaling. *Annu. Rev. Biophys.* **47**, 1–18 (2018).
39. Iiri, T., Bell, S. M., Baranski, T. J., Fujita, T. & Bourne, H. R. A Gsa mutant designed to inhibit receptor signaling through Gs. *Proc. Natl. Acad. Sci. U. S. A.* **96**, 499–504 (1999).
40. Sun, D. *et al.* Probing G α i1 protein activation at single-amino acid resolution. *Nat. Struct. Mol. Biol.* **22**, 686–694 (2015).
41. Flock, T. *et al.* Universal allosteric mechanism for G α activation by GPCRs. *Nature* **524**, 173–179 (2015).
42. Goricanec, D. *et al.* Conformational dynamics of a G-protein α subunit is tightly regulated by nucleotide binding. *Proc. Natl. Acad. Sci.* **113**, E3629–E3638 (2016).

Methods

No statistical methods were used to predetermine sample size. The experiments were not randomized and the investigators were not blinded to allocation during experiments and outcome assessment.

Preparation of NTR1 in cNDs

Expression and purification of a thermostable variant of rat NTR1 (TM86V-L167R DIC3B) was performed as described previously with some modifications^{29,43}. This NTR1 variant consists of residues G50-G390, contains a deletion of E273-T290 in intracellular loop (ICL) 3, and has ten stabilizing mutations. Briefly, the full-length fusion protein consisting of maltose-binding protein (MBP), NTR1, and thioredoxin (TrxA) was expressed in Tuner™ (DE3) Competent Cells (Novagen) in LB medium at 37 °C, 200 rpm and induced

at an OD₆₀₀ of 0.75 with 1 mM IPTG. Cells were grown for another 24 hours at 20 °C, 160 rpm and harvested by centrifugation (5,000 × *g*, 30 min, 4 °C). Cells were then lysed and solubilized by sonication in buffer containing 100 mM HEPES (pH 8.0), 20% glycerol, 400 mM NaCl, 2.5 mM MgCl₂, 0.6/0.12% CHAPS/cholesterol, 1.7% n-decyl-β-D-maltopyranoside (DM), 100 mg lysozyme, one tablet of protease inhibitor, and 250 U benzonase. Cell lysate was centrifuged, and the supernatant was mixed with pD-NT resin⁴³ pre-equilibrated with 25 mM HEPES (pH 8.0), 10% glycerol, 600 mM NaCl and 0.5% DM at 4 °C for 1 hour. The flow-through from the pD-NT resin was then discarded, and the resin was washed with 25 mM HEPES (pH 7.0), 10% glycerol, 150 mM NaCl, 2 mM DTT and 0.3% DM. The resin was then mixed with 3C protease for 1 hour at 4 °C to cleave off MBP and TrxA from NTR1, as well as NT-NTR1 from pD resin⁴³. The resin was washed with 10 mM HEPES (pH 7.0), 10% glycerol, 2 mM DTT and 0.3% DM, which was combined with the flow-through and loaded onto a SP cation exchange chromatography column (GE Healthcare) pre-equilibrated in the same washing buffer. The SP column was washed with 10 mM HEPES (pH 7.7), 10% glycerol, 35 mM NaCl, 2 mM DTT and 1% diheptanoylphosphatidylcholine (DH₇PC), and then eluted with 10 mM HEPES (pH 7.7), 10% glycerol, 350 mM NaCl, 2 mM DTT and 0.2% DH₇PC. The eluate was concentrated to below 500 mL and subjected to size-exclusion chromatography on a Superdex 200 10/300 Increase Analytical (S200a) column (GE Healthcare) equilibrated with 10 mM HEPES (pH 7.7), 150 mM NaCl, 2 mM DTT, 0.1% DH₇PC and 0.1 mM NT. Fractions containing NTR1 were collected and mixed with a 3:2 molar ratio of 1-Palmitoyl-2-oleoyl-phosphatidylcholine (POPC) to 1-palmitoyl-2-oleoyl-phosphatidylglycerol (POPG) solubilized in 100 mM sodium cholate at a NTR1:lipid molar ratio of 1:160. The mixture was incubated on ice for 30 min before addition of cNW9 at a cNW9:NTR1 molar ratio of 4:1 followed by another 30 min incubation on ice. The mixture was then treated with 5% volume of Bio-Bead SM-2 resin (Bio-Rad) with shaking on ice for 15 min, followed by addition of another 20% volume of Bio-Beads every 20 min for detergent removal. After two-hour incubation with Bio-Beads, the flow-through was then subjected to size-exclusion chromatography with a S200a column equilibrated in 20 mM sodium phosphate (pH 6.9), 50 mM NaCl, 1 mM DTT, 0.5 mM EDTA, 0.1 mM NT. Fractions containing NTR1-cND were concentrated to below 500 mL and incubated at 42 °C for 24 hours, followed by filtration through 0.22 mm cut-off filters. The flow-through was subjected to another round of size-exclusion chromatography. Fractions were pooled, concentrated and stored at 4 °C.

Preparation of Ga₁b₁g₁ in micelles and cNDs

G protein composed of Ga₁, Gb₁ and Gg₁ was expressed and purified as detailed before^{29,44}. Briefly, *Spodoptera frugiperda* (Sf9) were grown in suspension in ESF921 medium (Expression Systems, California), infected at a density of 2-3 × 10⁶/mL with a single baculovirus encoding all three subunits (Ga₁b₁g₁), harvested within 72 hours post inoculation, and stored at -80 °C until use.

Cells were lysed in 10 mM HEPES (pH 7.4), 20 mM KCl, 10 mM MgCl₂, 10 mM GDP, 2 mM b-mercaptoethanol (b-ME), and 1 protease inhibitor tablet with sonication. The suspension was then ultra-centrifuged at 180,000 × *g* for 45 min at 4 °C. The membrane pellet was solubilized in 50 mM HEPES (pH 7.4), 150 mM NaCl, 10 mM MgCl₂, 10 mM GDP, 2 mM b-ME, 10% glycerol, 1 protease inhibitor tablet, 1.2% DM at 4 °C for 3 hours. The suspension was ultra-centrifuged again and the supernatant was purified through Ni-NTA resin⁶. The eluate was concentrated and run through a Superdex 200 prep 16/60 column (S200p; GE Healthcare) equilibrated in 20 mM HEPES (pH 7.4), 100 mM NaCl, 0.1 mM MgCl₂, 4 mM b-ME, and 0.5% DM. Fractions containing Ga_{i1}b₁g₁ were pooled and concentrated to 10 mg/mL, flash-frozen in liquid nitrogen and stored at -80 °C.

Ga_{i1}b₁g₁-cNDs were prepared similarly as for NTR1-cNDs. After Bio-Bead removal, the Ga_{i1}b₁g₁-cNDs were purified through Ni-NTA to remove empty cNDs, followed by S200a chromatography to remove aggregates. Fractions containing pure Ga_{i1}b₁g₁-cNDs were collected, concentrated, and stored at 4°C.

Complex formation of NT-NTR1-Ga_{i1}b₁g₁ in cNDs

Purified Ga_{i1}b₁g₁ in micelle was diluted in buffer A (20 mM HEPES (pH 6.9), 50 mM NaCl, 5 mM CaCl₂, 1 mM DTT, 0.1 mM NT) until the DM concentration dropped below 0.08% (the critical micelle concentration of DM), and mixed with NTR1-cND at 1:1 molar ratio. The mixture was incubated on ice for 30 min, followed by addition of Bio-Beads at 10% volume every 30 min. The mixture was incubated on ice with shaking for a total of 2 hours and then the Bio-Beads were removed. Apyrase, diluted with buffer A and pretreated with Bio-Beads for 30 min on ice, was added to the complex at 1 U/mL concentration. The mixture was incubated at 4 °C overnight, and then subjected to a S200a SEC column equilibrated in 20 mM sodium phosphate (pH 6.9), 50 mM NaCl, 1 mM DTT, 0.5 mM EDTA, 0.1 mM NT. Peak fractions were characterized with SDS-PAGE and negative-stain EM. The fractions containing NT-NTR1-Ga_{i1}b₁g₁ in cNDs were used for cryo-EM structure determination.

Circular Dichroism (CD) spectroscopy

CD spectra were measured on a JASCO J-815 spectropolarimeter equipped with a Peltier cell temperature controller. Both spectrum scan measurement and variable temperature measurement were carried out for the following samples: NTR1 in micelles, NTR1-cNDs, Ga_{i1}b₁g₁ in micelles, Ga_{i1}b₁g₁-cNDs, and NTR1-Ga_{i1}b₁g₁ in cNDs. Spectrum scan measurements were performed at 20 °C, before and after variable temperature measurements, collecting data from 260 nm to 190 nm. Variable temperature measurements were carried out at 220 nm increasing temperature from 20 °C to 95 °C at a rate of 1 °C/min. *Spectrum Manager 2* software was used to analyze the transition temperature for each sample.

Binding affinity and kinetics measurement

Binding affinity and kinetics between NTR1 and Ga_{i1}b₁g₁ in detergent micelles and cNDs were measured using MicroScale Thermophoresis (MST) and Biolayer Interferometry (BLI).

For MST, the measurements were performed on a Monolith NT.115 system (NanoTemper Technologies). We measured the fluorescence signal from Ga_{i1}b₁g₁ by using the Monolith His-Tag Labeling Kit RED-tris-NTA 2nd Generation kit (NanoTemper Technologies). The samples were prepared in a buffer containing 20 mM sodium phosphate (pH 6.9), 50 mM NaCl, 0.05% DH₇PC for cND titrations and 0.2% DH₇PC for titrations in detergent micelle. The concentration of DH₇PC for cND titrations is below its critical micellar concentration. The experiments were carried out as fast as possible (within 1-2 minute for sample preparation) to prevent degradation of Ga_{i1}b₁g₁. The concentration of Ga_{i1}b₁g₁ was constant at 10 nM. NT-NTR1 in DH₇PC, NT-NTR1-cND, or empty cND was titrated in two-fold dilution steps beginning at 4 μM. For the measurement the samples were filled into premium-coated capillaries. The measurement was performed at 2 % LED and 20 % MST power, 30 sec Laser-On, and 5 sec Laser-Off. Fluorescence was excited at 605–645 nm, and emission was detected at 680–685 nm. The results were analyzed using the MO Affinity Analysis software (NanoTemper Technologies). The dissociation constant (K_D) was then determined using a single-site model for data fitting.

BLI experiments were performed on an Octet RED384 (ForteBio, California) using Anti-His antibody-coated Dip and Read Biosensors (HIS1, ForteBio) and 384 well plates (ForteBio) with 60 μL volume. 500 nM of His-tagged Ga_{i1}b₁g₁ was bound for 5 min in a binding buffer consisting of 20 mM HEPES (pH 7.4), 100 mM NaCl, 0.1 mM MgCl₂, 4 mM b-ME, and 0.5% DM. To test for nonspecific binding of His-tagged Ga_{i1}b₁g₁, reference tips were incubated in buffer alone. The tips were washed with buffer for 2 min to obtain a baseline reading and then transferred to wells in various concentrations of NT-NTR1-cND (4, 2, 1, 0.5, 0.25 μM) in buffer containing 20 mM sodium phosphate (pH 6.9), 50 mM NaCl, 1 mM DTT, 0.5 mM EDTA, 0.1 mM NT for 5 min. After measuring the association phase, tips were moved to wells containing buffer with and without GTPγS, and dissociation was measured for 5 min. The data were processed and analyzed using the Octet data analysis software version 11.0 (ForteBio). Association-dissociation curves for each concentration were fit to a 2:1 model.

Nuclear Magnetic Resonance (NMR) spectroscopy

Uniformly ^{15}N -labeled NT-NTR1 in POPC/POPG (3:2) cNW9 nanodiscs at 200 mM alone and in complex with unlabeled $\text{Ga}_{i1}\text{b}_1\text{g}_1$ at a molar ratio of 5:1 were prepared as described above in NMR buffer (20 mM sodium phosphate (pH 6.9), 50 mM NaCl, 1 mM DTT, 0.5 mM EDTA, 10% D_2O). Two-dimensional Transverse Relaxation Optimized Spectroscopy (TROSY) Heteronuclear Single Quantum Coherence (HSQC) were collected with 2000 scans, 200 increments at 45 °C on a Bruker 800-MHz spectrometer equipped with a TXO cryogenic probe. TROSY HSQC measurements were repeated for NT-NTR1-cND on an Agilent 700-MHz spectrometer to verify that NT-NTR1-cND stays intact after long data acquisition in the magnet at 45 °C. Data were processed using the NMRPipe software package⁴⁵.

Functional Assay

Ligand-induced IP1 (a metabolite of IP3) accumulation was measured in transiently transfected HEK293T/17 cells as described before⁴⁶. Wild type rNTR1 or mutants thereof were directly subcloned into a mammalian expression vector containing an N-terminal SNAP-tag (pMC08). 24 hrs after transfection, cells were washed with PBS, detached with Trypsin-EDTA (Sigma) and resuspended in assay buffer (10 mM HEPES pH 7.4, 1 mM CaCl_2 , 0.5 mM MgCl_2 , 4.2 mM KCl, 146 mM NaCl, 50 mM LiCl, 5.5 mM glucose, 0.1% (w/v) BSA). Cells were seeded at 20,000 cells per well in white 384-well plates (Greiner) and incubated for 2 hrs at 37 °C with a concentration range of NT_{8-13} (Anawa) diluted in assay buffer. IP1 accumulation was measured using the HTRF IP-One kit (Cisbio) according to the manufacturer's protocol. To confirm cell surface expression of NTR1 and its mutants, transfected cells were plated on poly-D-lysine treated 384-well plates (Greiner) at 20,000 cells/well in growth medium. The following day, medium was removed and cells were incubated with 50 nM SNAP-Lumi4-Tb (CisBio) in labelling buffer (CisBio) for 2 hrs at 37 °C. Thereafter, cells were washed 4 times with wash buffer (20 mM HEPES pH 7.5, 100 mM NaCl, 3 mM MgCl_2 and 0.2% (w/v) nonfat milk). Fluorescence intensity of Tb^{3+} -labelled receptors was measured on an Infinite M1000 fluorescence plate reader (Tecan) with an excitation wavelength of 340 nm and emission wavelength of 620 nm. To generate concentration-response curves, data were normalized to receptor expression at the cell surface and to response of NTR1 at maximal ligand concentration and were analysed by a non-linear curve fit in GraphPad Prism.

Negative-stain microscopy

3 μL of NT-NTR1- $\text{Ga}_{i1}\text{b}_1\text{g}_1$ -cND complex at a concentration of 0.02 mg/mL was applied onto a glow-discharged continuous carbon grid (Electron Microscopy Sciences, Inc.). After two minutes of adsorption, the grid was blotted with filter paper to remove the excess sample, immediately washed twice with 50 μL of MiliQ water, once with 50 μL 0.75% uranyl formate solution and incubated with 50 μL of 0.75% uranyl formate solution for an additional one minute. The grid was then further blotted with filter paper to remove the uranyl formate solution, air-dried at room temperature, and examined with a Tecnai T12

electron microscope (Thermo Fisher Scientific) equipped with an LaB6 filament and operated at 120-kV acceleration voltage, using a nominal magnification of 52,000 \times at a pixel size of 2.13 Å.

Cryo-EM sample preparation

Cryo-EM grids were prepared using a Vitrobot Mark IV (Thermo Fisher Scientific). 3 mL of NT-NTR1-Ga_{i1}b₁g₁-cND at a concentration between 1.5 mg/mL to 1.7 mg/mL was applied onto glow discharged C-flat holy carbon grids (R1.2/1.3, 400 mesh copper, Electron Microscopy Sciences) or Quantifoil holy carbon grids (R1.2/1.3, 400 mesh gold, Quantifoil Micro Tools). The grids were blotted for 7.5 s with a blot force of 16 and 100% humidity before being plunged into liquid ethane cooled by liquid nitrogen.

Cryo-EM data collection

Images of NT-NTR1-Ga_{i1}b₁g₁-cND were acquired on Titan Krios I at the Harvard Cryo-EM Center for Structural Biology equipped with a BioQuantum K3 Imaging Filter (slit width 20 eV) and a K3 direct electron detector (Gatan) and operating at an acceleration voltage of 300 kV. Images were recorded at a defocus range of -1.2 μ m to -2.5 μ m with a nominal magnification of 105,000 \times , resulting in a pixel size of 0.825 Å. Each image was dose-fractionated into 38 movie frames with a total exposure time of 1.5 s, resulting in a total dose of \sim 57 electrons per Å². SerialEM was used for data collection⁴⁷.

Image processing

A total of 23,677 movie stacks, which were collected during two sessions, were motion corrected and electron-dose weighted using MotionCor2 (ref.⁴⁸). Parameters of the contrast transfer function were estimated from the motion-corrected micrographs using CTFFIND4 (ref.⁴⁹). To generate a reference, particles from 10 micrographs were picked manually in EMAN2.2 (ref.⁵⁰), crYOLO⁵¹ was then trained for picking particles automatically. All subsequent 2D and 3D analyses were performed using RELION-3.0 or RELION-3.1-beta⁵².

1,726,457 particles were selected after several rounds of 2D classification from 4,367,542 auto-picked particles. Density map of the human NTR1 in complex with the agonist JMV449 and the heterotrimeric G_{i1} protein (EMDB-20180)⁸ was low-pass filtered to 20 Å and used as the initial model for the first round of 3D classification, yielding five different classes. Two classes of the NT-NTR1-Ga_{i1}b₁g₁-cND complex were relatively better resolved and particles from these two classes were subject to 3D refinements. Bayesian polishing was then performed, followed by 3D refinement and post-processing, yielding two

density maps at resolutions of 4.3 Å (canonical state) and 4.5 Å (noncanonical state), respectively. To further improve the resolution of the core of the complex, masks excluding the nanodisc and the AHD were applied during the 3D refinement, yielding the 4.1 Å (canonical state) and 4.2 Å (noncanonical state) density maps, respectively. Per-particle CTF refinement was performed but did not lead to an improvement in map resolution or quality.

Model building and refinement

The crystal structures of NT-NTR1 complex (PDB: 4BUO)²⁹ and G protein heterotrimer Ga_{i1}b₁g₂ (PDB: 1GP2)²⁸ and the cryo-EM structure of Ga_Tb₁g₁ (PDB: 6OY9)³² were fitted into the density map of the canonical NT-NTR1-Ga_{i1}b₁g₁-cND complex using the Fit in Map function of Chimera⁵³. The a_{i1}b₁ subunits of Ga_{i1}b₁g₂ and g₁ subunit of Ga_Tb₁g₁ were merged with the NT-NTR1 structure and the amino acids were modified in Coot version 0.9-pre to match our constructs⁵⁴. The amino acids F291-R299 of NTR1 of the canonical state were mutated to poly-alanine due to the lack of sidechain densities. The model was manually adjusted and refined in Coot with torsion, planar peptide, trans peptide and Ramachandran restraints applied. For the noncanonical state, the subunits of the refined atomic model of the canonical state were fitted into the density map as separate rigid bodies. The model was manually adjusted and refined in Coot. For both states, the AHD was extracted from the crystal structure of the human Ga_{i1} (PDB: 3UMR) and docked into the density as a rigid body using Chimera.

Models were refined with Phenix.real_space_refine⁵⁵. The AHD was not refined due to the lack of sidechain information for this domain. During refinement, the resolution limit was set to match the map resolution determined by the FSC=0.143 criterion in post-processing. Secondary structure, Ramachandran, rotamer, and reference restraints from the JMV449-NTR1-G_i-scFv16 complex (PDB 6OS9)⁸ were applied throughout refinement. The final models were validated using MolProbity v.4.3.1 (ref.⁵⁶) with model statistics provided in Table S1.

Molecular dynamics simulations

The molecular system for the molecular dynamics (MD) simulations was prepared based on the canonical state structure of NT-NTR1-Ga_{i1}b₁g₁-cND which was preprocessed with Maestro from Schrödinger^{57,58}. Bond orders were assigned, hydrogens added, disulfide bonds created, and het states generated at pH 7.0±2.0. The sidechains of residues 291 to 299 were assigned and the truncated residues 273 to 290 in NTR1 construct were added with the Crosslink Proteins tool of Maestro^{57,58}.

The membrane and solvent environment, as well as the input files for Amber were generated using the Membrane Builder tool of CHARMM-GUI^{59,60}. The terminal groups of each chain were patched with standard N-terminus and C-terminus patch residues, except for the N-terminus of Ga for which a GLYP patch residue was used. For orienting the complex appropriately, the PPM (Positioning of Proteins in Membrane) server of the OPM (Orientations of Proteins in Membranes) database was used⁶¹. A lipid bilayer containing a total of 527 lipids, composed of a 3:2 molar ratio of POPC to POPG, was added to the aligned complex with Membrane Builder^{59,60}. A rectangular solvation box was added by adding water layers of at least 22.5 Å above and below the membrane. The system was ionized and neutralized by adding 50 mM of sodium and chloride ions. The resulting system contained a total of 286,109 atoms.

In total, 12 simulations of the prepared system were run using Amber18 (ref.⁶²). The Amber FF14SB⁶³ and Amber Lipid17 (ref.⁶⁴) force fields were used for the proteins and the lipid bilayer, respectively. The TIP3P model⁶⁵ was used for the water molecules. During the energy minimization, 2500 steps of steepest descent followed by 2500 steps of conjugate gradient were carried out. The equilibration steps were carried out according to the standard Membrane Builder protocols⁶⁶. The production MD simulations were carried out at 310 K and 1 bar in an NPT ensemble using a Monte Carlo barostat and a Langevin thermostat. The cutoff for the nonbonded interactions was set to 10 Å, and the particle mesh Ewald method was used for the long-range electrostatic interactions. Hydrogen mass repartitioning was enabled, and a time step of 4 fs applied. Postprocessing was carried out with AmberTools 18 and VMD 1.9.4 (ref.⁶²) The simulation lengths of the runs were between 600 ns and 1 μs.

Declarations

Acknowledgments

Cryo-EM data were collected at the Harvard Cryo-Electron Microscopy Center for Structural Biology. We thank F. Koh, P. Egloff, P. Heine, M. Hillenbrand, and J. Schöppe for their contribution to the early stages of this project, S. Sterling, R. Walsh, and Z. Li for microscopy support, SBGrid for computing support, M. Deluigi for supervising the signaling experiments, and R. Walker, K. Bayer, P. Imhof and M. Bagherpoor for their advice and discussions regarding the molecular dynamics simulations. M.G. is supported by a Merck-BCMP fellowship. A.B. is supported by the International Retinal Research Foundation, the E. Matilda Ziegler Foundation for the Blind, the Richard and Susan Smith Family Foundation, and the Pew Charitable Trusts. We acknowledge support by NIH grants GM129026 and AI037581 to G.W. and GM131401 to M.L.N. G.W. and A.P. are supported by HFSP RGP0060/2016. A.P. is supported by Swiss National Science Foundation grant 31003A_182334.

Competing interests:

M.L.N. and G.W. founded the company NOW Scientific to sell assembled cNDs, but a plasmid for expressing the NW9 membrane scaffolding protein is available through the Addgene plasmid depository (catalog number 133442) for academic/nonprofit institutions. Otherwise, the authors declare no competing interests.

Data and materials availability

Structural data have been deposited into the Worldwide Protein Data Bank (wwPDB) and the Electron Microscopy Data Bank (EMDB). The EM density maps for the canonical and noncanonical states of NT-NTR1-G_i complex in lipid nanodiscs have been deposited under accession codes EMD-XXXX and EMD-XXXX. The masked EM density maps excluding the nanodisc and AHD of the canonical and noncanonical states have been deposited under accession codes EMD-XXXX and EMD-XXXX. The corresponding atomic models have been deposited under accession codes YYYYY and YYYYY. Other data are available upon reasonable request.

Author contributions:

M.Z. developed the protocol for making NT-NTR1-G_{α₁β₁γ₁}-cND complexes, prepared samples, collected negative-stain EM images, and performed biophysical experiments. M.G. prepared cryo-EM grids, obtained and processed the data, and built and refined the atomic models. M.Z. and Z.W. performed binding experiments. C.G. performed MD simulations. J.Y. expressed G_{α₁β₁γ₁}. H.W. obtained and processed cryo-EM data. M.Z. and J.S. performed NMR experiments. C. K., L. Me and L. Mo made constructs and performed signaling experiments. A.P. designed and supervised the signaling experiments. F.H. and G.W. initiated the project. A.B., M.L.N., and G.W. designed and supervised the project. M.Z. wrote the paper. M.Z., M.G., Z.W., C.G., J.Y., C. K., A.P., A.B., M.L.N., and G.W. edited the paper.

Tables

Extended Data Table 1. Cryo-EM data collection, refinement and validation statistics

	NT-NTR1-G ₁ -cND Canonical state (EMDB-xxxx) (PDB xxxx)	NT-NTR1-G ₁ -cND Noncanonical state (EMDB-xxxx) (PDB xxxx)
Data collection and processing		
Magnification	105,000	105,000
Voltage (kV)	300	300
Electron exposure (e ⁻ /Å ²)	57	57
Defocus range (µm)	-1.2 to -2.5	-1.2 to -2.5
Pixel size (Å)	0.825	0.825
Symmetry imposed	C1	C1
Initial particle images (no.)	4,367,542	4,367,542
Final particle images (no.)	575,791	324,002
Map resolution (Å)	4.1	4.2
FSC threshold	0.143	0.143
Refinement		
Refinement software	Coot 0.9-pre, Phenix-dev-3318	
Initial model used (PDB code)	4BUO, 1GP2, 6OY9	
Resolution limit set in refinement (Å)	4.1	4.2
Map sharpening <i>B</i> factor (Å ²)	-245	-204
Model composition		
Non-hydrogen atoms	6959	6979
Protein residues	883 (6901 atoms)	882 (6921 atoms)
Ligands	1 (6 residues, 58 atoms)	1 (6 residues, 58 atoms)
<i>B</i> factors (Å ²)		
Protein	73.57	73.56
Ligand	66.76	66.76
R.m.s. deviations		
Bond lengths (Å)	0.006	0.007
Bond angles (°)	1.052	1.365
Validation		
MolProbity score	1.90	1.96
Clashscore	8.36	9.77
EMRinger score	1.46	1.17
Poor rotamers (%)	0.53	1.05
Ramachandran plot		
Favored (%)	93.11	93.33
Allowed (%)	6.89	6.67
Disallowed (%)	0	0

Figures

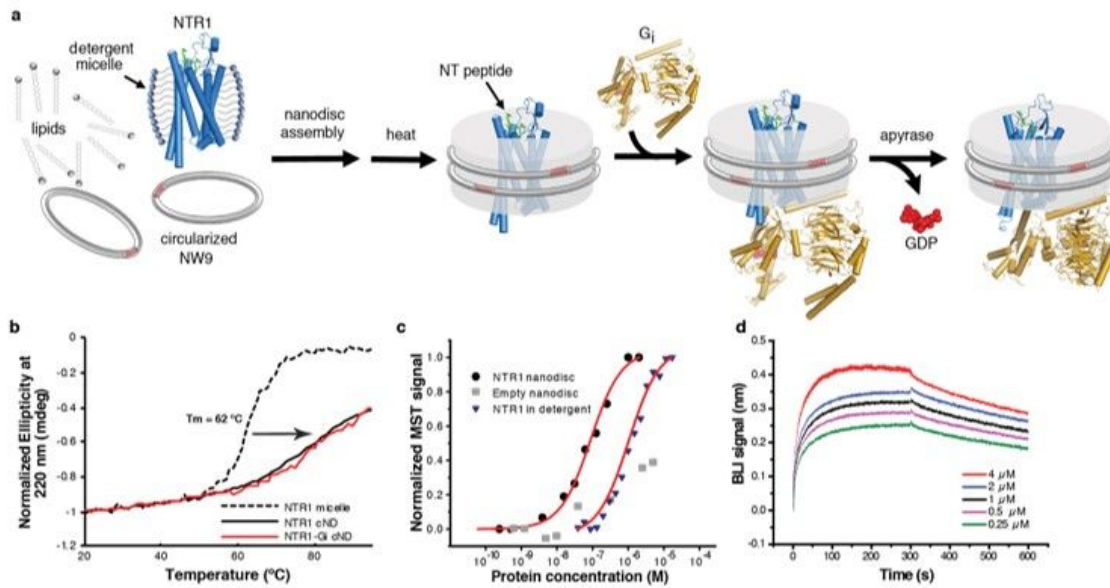


Figure 1

Assembly and biophysical characterization of the NT-NTR1-Gi complex in circularized nanodiscs (cNDs). a, Schematic showing the assembly of the NT-NTR1-Gi complex in lipid nanodiscs using the circularized membrane scaffold protein cNW9. b, Circular dichroism thermostability assays on NT-NTR1 in detergent micelles (dashed black line) with NT-NTR1 (solid black line) and NT-NTR1-Gi complex (solid red line) in cNDs. c, Microscale thermophoresis data fitting for the interaction between NT-NTR1 and Gi in diheptanoylphosphatidylcholine detergent (DH7PC) yields a K_D of 1400 ± 100 nM (blue triangles). The interaction between NT-NTR1-cND and Gi (black circles) yields a K_D of 76 ± 18 nM. Weak binding between empty nanodiscs and Gi is shown as gray squares. d, Bio-layer interferometry (BLI) traces of Gi binding to NT-NTR1-cND at five different concentrations. Data fitting results are shown in Extended Data Fig. 4a, b.

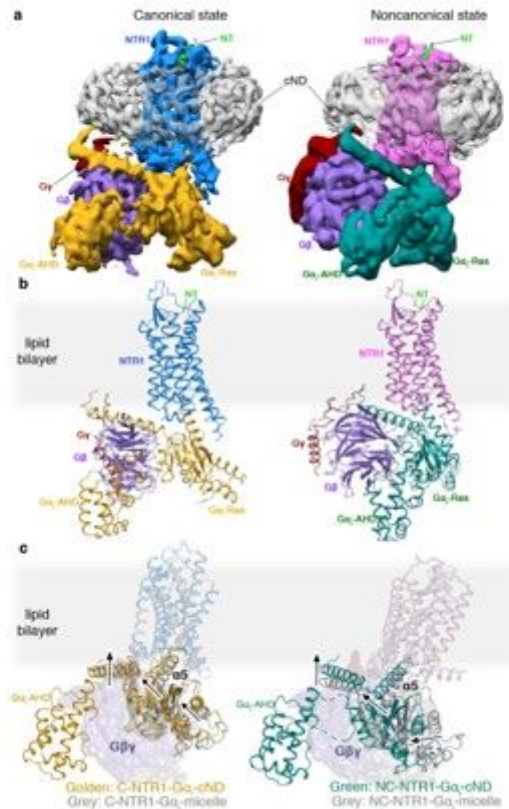


Figure 2

Cryo-EM structures of NT-NTR1-Gi-cND. a, Cryo-EM density maps of NT-NTR1-Gi-cND complex in the canonical state (left) and in the noncanonical state (right). The maps are low-pass filtered to 5 Å and colored by subunit. Higher-resolution maps were obtained by masking out density for the nanodisc and G $\beta\gamma$ AHD domain. b, Atomic models of NT-NTR1-Gi-cND complex in the canonical state (left) and in the noncanonical state (right). The models are shown in the same orientation as the maps in (a). c, Structural superimposition of C-NT-NTR1-Gi-cND with C-NTR1-scFv16-micelle (left) and NC-NT-NTR1-Gi-cND with NC-NTR1-scFv16-micelle (right). Structural displacement is highlighted with arrows. The models are superimposed on the NTR1.

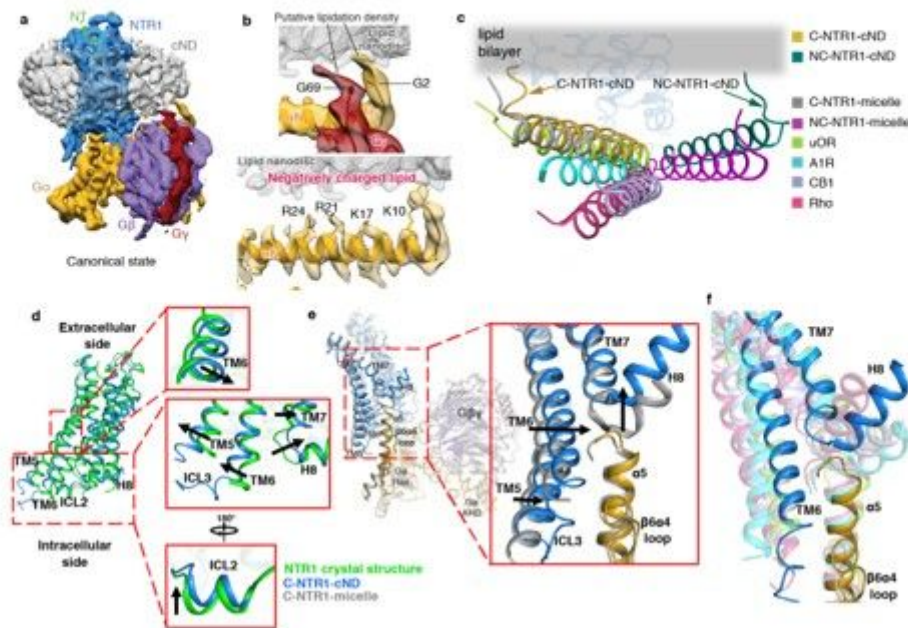


Figure 3

Impact of lipid bilayer on the NTR1-Gi complex. a, Cryo-EM density map of the NT-NTR1-Gi-cND complex in the canonical state. The map is low-pass filtered to 5 Å to aid visualization and colored by subunit. b, Top panel, density for the putative lipid modifications of glycine 2 (G2) of G α 11 and glycine 69 (G69) of G α 11. Nanodisc density is shown as gray mesh. The density map of the canonical state is low-pass filtered to 5 Å. Bottom panel, positively charged residues of the α N helix of G α 11 face the negatively charged lipid bilayer. The 4.1 Å density map of the canonical state is shown. c, Comparison of the α N helices of GPCR-Gi complexes. C-NTR1-cND and NC-NTR1-cND indicate the canonical and noncanonical states of the NT-NTR1-Gi complex in lipid nanodiscs. C-NTR1-micelle and NC-NTR1-micelle indicate the canonical and noncanonical states of JMV449-NTR1-Gi complex in detergent micelles. Other Class A GPCR-Gi complexes: μ OR-Gi (lime green; PDB 6DDE), A1R-Gi (cyan; PDB 6D9H), CB1-Gi (purple; PDB 6N4B), and Rho-Gi (hot pink; PDB 6CMO). The models are superposed on the GPCR. d, Structural comparison between NTR1 from the canonical state NT-NTR1-Gi complex in lipid nanodiscs (blue) and the crystal structure of NTR1 in detergent (green). Zoomed-in views are shown on the right. e, Structural comparison between the canonical states of NTR1-Gi in lipid bilayer (blue) and detergent (gray), superposed on the Ras-like domain of G α (gold). Zoomed-in view of the cytoplasmic side of TM5-TM6, ICL3, TM7-H8, as well as the α 5 helix and α 6 α 4 loop of G α is shown on the right. f, Comparison of the location of TM6 relative to the α 5 helix of G α in the canonical state NTR1 (blue) in complex with Gi (gold) with other class A GPCR-Gi complex structures, including the canonical state of NTR1-Gi in detergent micelle (gray), μ OR-Gi (lime green), Rho-Gi (hot pink), A1R-Gi (cyan), and CB1-Gi (purple). The models are superposed on the Ras-like domain of G α .

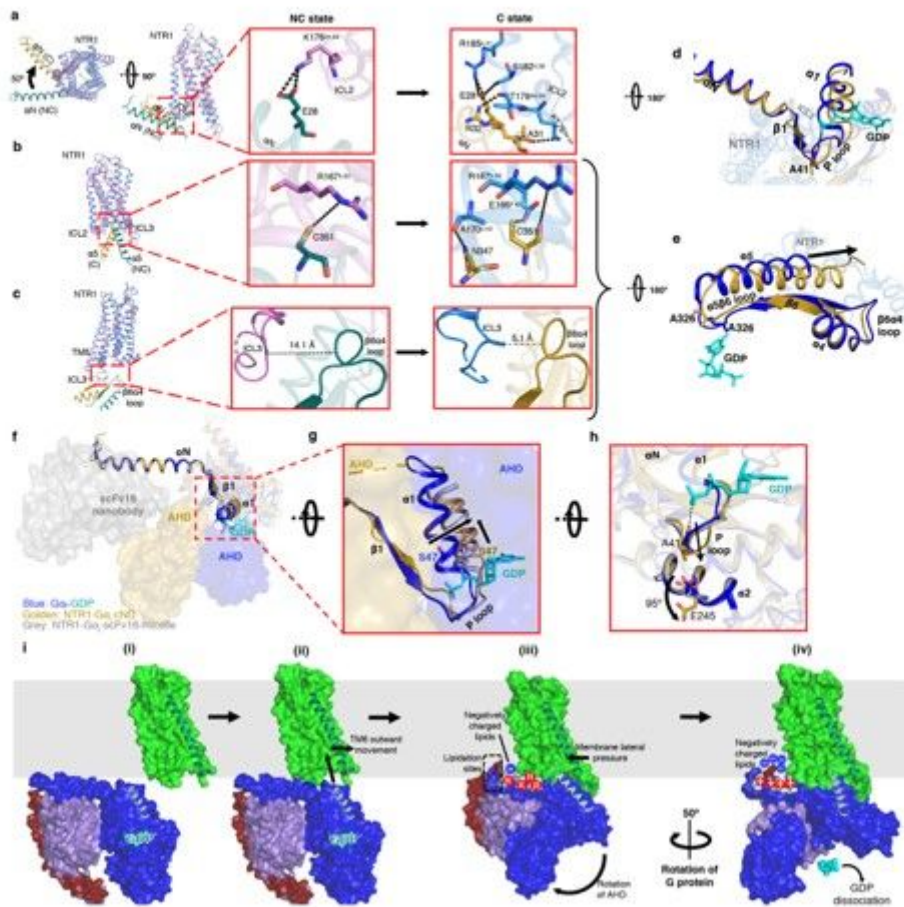


Figure 4

Allosteric modulation of the GDP binding pocket by the NTR1-Gi interaction. a-c, Superposition between C-state NTR1 (blue) and α N helix of G α (gold) with the NC-state NTR1 (orchid) and α N helix of G α (dark cyan). Models are superposed on NTR1. Overview (left) and zoomed-in views of the NC state (middle) and C state (right) are shown. a, ICL2- α N helix interactions. Compared to the NC state, the α N helix of G α of the C state is rotated by 50°. b, NTR1- α 5 helix interactions. c, ICL3- α 6 α 4 loop interactions. The backbones of ICL3 and α 6 α 4 are closer in the C state and form interactions predicted by molecular dynamics simulations (Extended Data Fig. 11a). d, Intracellular view showing perturbation of the P loop in the C state (gold) relative to the crystal structure of GDP-bound Gi (blue; GDP in cyan). e, Intracellular view showing perturbation of the α 5 α 6 loop in the C state (gold) relative to the crystal structure of GDP-bound Gi (blue; GDP in cyan). In d-e, the models are superposed on the G α Ras-like domain. f, Structures of GDP-bound G α i (blue; GDP in cyan), NTR1-bound G α i in detergent (grey) and NTR1-bound G α i in lipid bilayer (gold) showing the different locations of the AHD and the stabilizing antibody scFv16. The structures are superposed on α N- α 1. g, Zoom-in view showing lateral displacement of α 1 helix including S47 from the phosphates of GDP in NTR1-Gi-cND. h, Rotation of E245 in NT-NTR1-Gi-cND (gold) by 95° compared to the GDP-Gi structure (blue) to accommodate the P-loop. This structural change is not observed in detergent (grey). i, Model of the proposed insertion-rotation mechanism: (i) Lateral diffusion of NTR1 and

Gi in the membrane; (ii) Recognition of NTR1 by Gi, allowing insertion of $\alpha 5$ into the open cavity of NTR1; (iii) Formation of the NC state including displacement of the AHD; (iv) Formation of the C state following rotation of Gi.

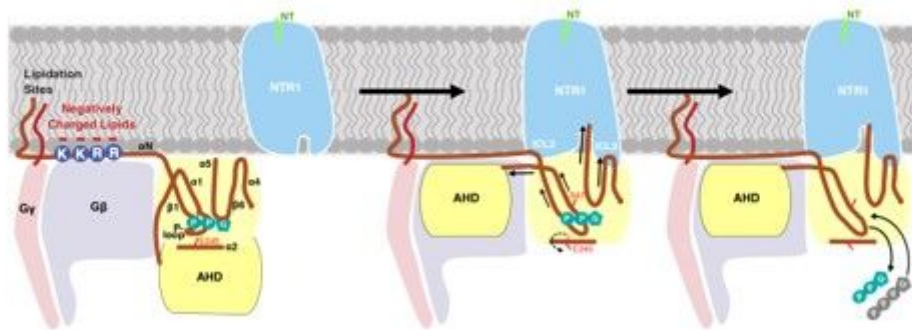


Figure 5

Proposed mechanism of GDP release. The interaction between Gi and NTR1 leads to allosteric modulation of the GDP-binding site via three pathways: (1) The movement of the AHD to G α perturbs the directly linked $\alpha 1$, resulting in $\alpha 1$ dissociation from the phosphate groups of GDP; (2) The interaction between ICL2 of NTR1 and αN - $\alpha 1$ hinge of G protein perturbs the P-loop through $\alpha 1$, resulting in P-loop dissociation from the phosphate groups of GDP, which is coupled with a 95° rotation of the sidechain of E245 on $\alpha 2$; (3) The interactions between $\alpha 5$ and core of NTR1 and between $\alpha 6$ $\alpha 4$ loop and ICL3 pull the $\alpha 5$ $\alpha 6$ loop away from the guanine ring of GDP. The multi-point coordination of these structural elements leads to dissociation of both the phosphates and the guanine ring of GDP from Gi, and thus dissociation of the entire GDP. Release of GDP vacates the nucleotide-binding pocket for subsequent GTP binding, thus completing the GDP/GTP exchange process.

Supplementary Files

This is a list of supplementary files associated with this preprint. Click to download.

- [PDBvalidationreportNCstate.pdf](#)
- [PDBvalidationreportCstate.pdf](#)
- [Suppfigures.docx](#)